Defect tolerance of intersubband transitions in nonpolar GaN/AlGaN heterostructures: A path toward low-cost and scalable mid- to far-infrared optoelectronics

Morteza Monavarian[1,2,†,*], Jiaming Xu[3,†], Michel Khoury[2], Feng Wu[1,2], Philippe De Mierry[4], Philippe Vennegues[4], Mikhail A. Belkin[3,5,*], James S. Speck[1,2,*]

[1]*Materials Department, University of California, Santa Barbara, California 93106, USA*
[2]*Solid-State Lighting Energy Electronic Center (SSLEEC), University of California Santa Barbara, California 93106, USA*
[3]*Electrical and Computer Engineering Department, University of Texas, Austin, Texas 78758, USA*
[4]*CNRS, Université Côte d'Azur, CRHEA, Rue Bernard Gregory, 06560 Valbonne, France*
[5]*Walter Schottky Institute, Technical University of Munich, Am Coulombwall 4, 85748 Garching, Germany*
[†]*These authors contributed equally to this work.*

** Corresponding Authors** mmonavarian@ucsb.edu , mikhail.belkin@wsi.tum.de, speck@ucsb.edu

KEYWORDS. GaN, AlGaN, Nonpolar, Intersubband, Quantum Well, Structural Defects, Stacking Faults, Dislocations, Heteroepitaxy, Surface Morphology, Interface Abruptness, Alloy Disorder, Infrared, Optoelectronics

ABSTRACT

We report on the impact of structural defects on mid-infrared intersubband (ISB) properties of GaN/AlGaN heterostructures grown by ammonia molecular beam epitaxy (NH_3-MBE). 20-period GaN/AlGaN multi-quantum well (MQW) heterostructures were grown on co-loaded *a*-plane freestanding GaN substrates and heteroepitaxial *a*-plane GaN on *r*-plane sapphire templates (*a*-GaN/*r*-Sap) for three different quantum well (QW) widths (3.0, 3.3, and 3.7 nm). Co-loaded

structures grown on freestanding *a*-plane with no basal-plane stacking faults (BSFs), prismatic stacking faults (PSFs), and partial dislocation (PDs), with low threading dislocation (TD) densities of ~ 10^5 cm^{-2} were compared with those grown on *a*-GaN templates on $(10\bar{1}2)$ *r*-sapphire with BSF, PSF, PD and TD densities of ~ 4×10^5 to 10^6 cm^{-2}, 5×10^3 to 2×10^4 cm^{-2}, ~ 9×10^{10} to 2×10^{11} cm^{-2} and ~ 10^{10} cm^{-2}, respectively. The Fourier transform infrared absorption spectroscopy indicates ISB transition energies in the range of ~250–300 meV (wavelength range 4.1–4.8 μm) for MQWs with different QW widths. The ISB absorption spectra indicate ~ 5% smaller transition energies and only ~ 10-20% larger spectral linewidths for the structures grown on *a*-GaN/*r*-sapphire templates compared to those on freestanding GaN substrates. The strong defect tolerance in the nonpolar *a*-plane ISB structures can be due to the nature of defects and their energy levels with respect to the conduction band minima, which is not affecting ISB properties. Our results can pave the way toward production of low-cost scalable nonpolar III-nitride MQW heterostructures for a variety of passive and active optical materials and devices based on intersubband transitions.

1. INTRODUCTION

Since the discovery and implementation of the first quantum cascade lasers (QCLs) in the mid-90s [1], the intersubband (ISB) transitions have been widely considered for mid-infrared (mid-IR, $\lambda \approx$ 3-30 μm) and terahertz (THz, $\lambda \approx$ 30-300 μm) devices for various applications, including biological imaging, telecommunications, pharmaceutical quality control, and security screening [2,3]. Unlike conventional semiconductor lasers [4] that rely on recombination of electron-hole pairs via band-to-band transitions, QCLs are unipolar devices with lasing obtained via intersubband (ISB) transitions in a stack of multi-quantum well (MQW) heterostructures [5].

THz QCLs based on arsenide and phosphide systems face issues with small longitudinal optical (LO) phonon energies [6] especially for higher frequencies (5-10 THz). III-nitrides, on the other hand, have the advantage of large LO phonon energy (~ 92 meV) [7], which makes it potentially more favorable for room temperature QCLs across the entire THz spectral range [8,9]. In addition, due to the large band offsets [7,10,11], III-nitrides may possibly provide access to ranges of wavelengths inaccessible to devices and optical materials based on intersubband transitions in the arsenide and phosphide based materials systems [12].

Nonlinear optical and electro-optic elements based on ISB transitions [13–20] can also benefit from wider accessible range of wavelengths provided by the high-conduction-band-offset III-nitride systems. To enhance optical nonlinearities, using wave-guiding schemes [21,22], metallic nanoantenna arrays [23], and nonlinear metasurface-based flat optical components [15–17,24,25] has received increasing attention. In particular, the introduction of sub-wavelength thickness nonlinear metasurfaces provided a path toward efficient frequency mixing without the need for phase-matching limitations of bulk nonlinear crystals [26] and with controlled output beam phase front [17,27]. Application of QCLs and nonlinear frequency conversion, such as second harmonic generation (SHG) [18,19], sum frequency generation (SFG) [20], and difference frequency generation (DFG) [20] with enhanced nonlinearities in III-nitride based systems can provide light sources in wide ranges of wavelengths from near- to far-IR.

Conventional III-nitride materials on polar (0001) orientation (*c*-plane) faces various limitations due to the strong polarization-induced internal electric field [28]. The electric field across the active QWs in ISB structures can markedly reduce electron wavefunction overlap [29,30], ISB transition oscillator strength, and thus transition efficiency [12,31,32]. In addition, the polarization-related electric field normally distorts the band profiles to shape

triangular QWs, resulting in the escape of electrons from the active region [32]. Nonpolar crystal orientation of III-nitrides (Figure 1(a)) with suppressed polarization-related electric field is an alternative to eliminate the abovementioned issues with conventional polar orientation [12,28].

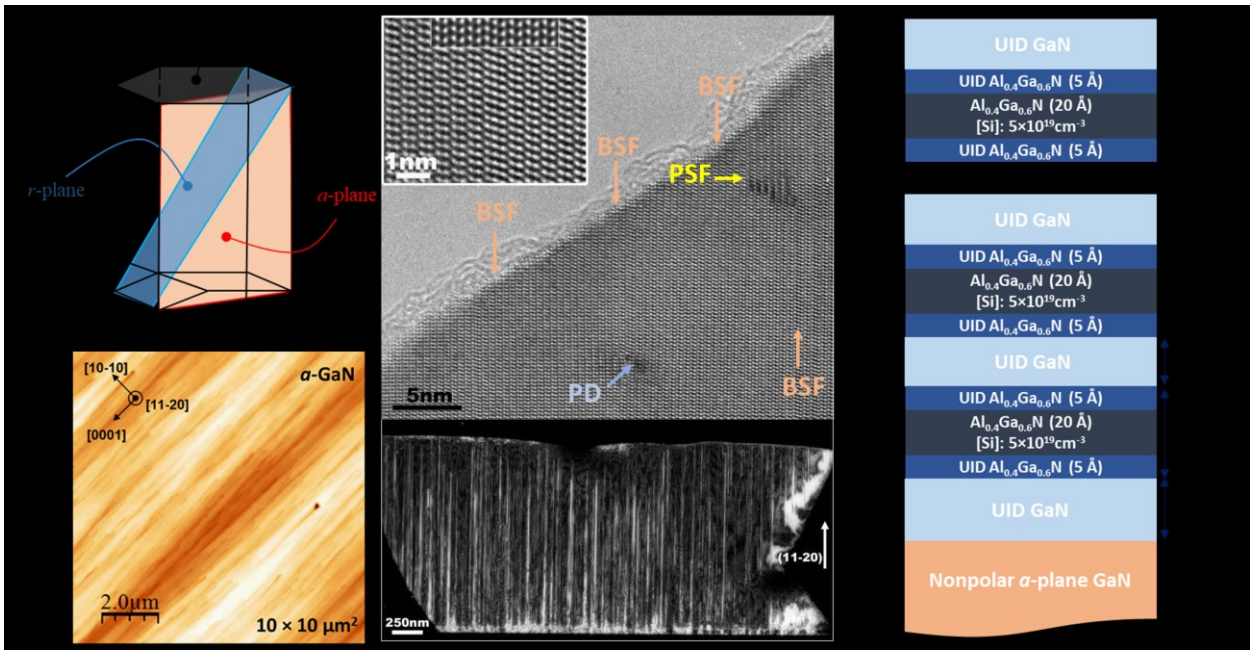

Figure 1. (a) Schematic representation of selected crystal planes in wurtzite crystal structure of III-nitrides, indicating polar *c*-plane, semipolar $\{10\bar{1}2\}$ *r*-plane, and nonpolar $\{11\bar{2}0\}$ *a*-plane. (b) Plan-view (top) high-resolution transmission electron microscopy (TEM) image of the *a*-GaN/*r*-Sap template along the $[11\bar{2}0]$ zone axis, showing the dominant defects are basal-plane stacking faults (BSFs) which are indicated by orange arrows. BSFs may either be terminated by partial dislocation (PDs) (pale blue arrows), or two neighboring BSFs may be connected by a $(11\bar{2}0)$ PSF (yellow arrow). Bottom of (b) shows a cross sectional image of PDs which are vertically threading from the interface to the surface. (c) Representative surface of *a*-plane orientation of GaN indicating elongated features toward *c*-direction. (d) Schematic structure of *a*-plane GaN/AlGaN ISB structures used in this study. Note that the monolayer thickness for GaN is ~ 0.25 nm.

There are different reports of nonpolar III-nitrides (either $\{10\bar{1}0\}$ family of *m*-planes and the nonpolar $\{11\bar{2}0\}$ family of *a*-planes) for ISB applications [31,33–37]. We recently reported a record narrow ISB absorption linewidth ~ 38 meV at 4.5 – 5.5 μm on nonpolar $(10\bar{1}0)$ (*m*-plane) freestanding substrates and systematically compared the two nonpolar planes for ISB applications [12,38]. Most of the reported nonpolar III-nitride ISB properties have been on freestanding substrates, which are extremely expensive and small in size [28,39,40]. The lack of

high-quality inexpensive nonpolar substrates has been a bottleneck in the regular band-to-band based applications, such as light-emitting diodes (LEDs), and lasers [28]. However, thus far, there is no clear indication as to whether ISB properties is similarly affected by the presence of extended defects compared to the band-to-band transitions, especially since most of the extended defects cause the nonradiative centers as states within the bandgap and, thus may not affect the ISB structures, which are unipolar in nature.

In this report, we systematically compare ISB transition properties of GaN/AlGaN MQW heterostructrues on nonpolar *a*-plane orientation on substrates with low and high defect densities.

2. EXPERIMENTAL DETAILS

The structures were all grown by a Gen 930 ammonia molecular-beam epitaxy (NH_3-MBE) where NH_3 decomposition at elevated temperatures provide elemental N for growth of GaN and its alloys. In the NH_3-MBE system, Ga, Al effusion cells were used to provide metallic elements and Si effusion cell for Si *n*-type dopant. Two sets of samples were considered. The first set of samples use *a*-GaN freestanding (*a*-GaN-FS) from Mitsubishi Chemical Corporation (MCC) with no BSFs, PSFs, and PDs, and a TD density of ~ 10^5 cm^{-2}. The second set of samples utilized heteroepitaxial *a*-plane GaN templates grown on *r*-plane sapphire (*a*-GaN/*r*-Sap) (the most commonly used foreign substrate for the growth of nonpolar GaN). The heteroepitaxy of *a*-GaN/*r*-Sap templates were carried out by metal-organic chemical vapor deposition (MOCVD) in a close-coupled showerhead reactor using trimethylgallium (TMG) and NH_3 as precursors and hydrogen (H_2) as the main carrier gas. 0.85 μm-thick *a*-plane GaN templates were grown on *r*-plane sapphire. The epitaxial process began with sapphire nitridation at 1120 °C and a low temperature GaN buffer

deposition at 690 °C at 100 Torr, followed by buffer annealing and 3D crystal formation at 1200 °C and 700 Torr and crystal expansion at 1090 °C and 300 Torr before the final coalescence step at 1200 °C and 10 Torr.

The microstructure of nonpolar heteroepitaxial films is very different from those deposited along the polar *c*-direction, which is dominated by the presence of vertically threading perfect dislocations mainly of *a*-type (edge) and *a* + *c* type (mixed). Even though the densities and nature of extended defects in heteroepitaxial nonpolar GaN may be a bit different depending on the substrates, similar general trends are observed for nonpolar *a*-GaN/*r*-Sap layers. Figure 1(b) shows a high-resolution cross-sectional transmission electron microscopy (TEM) image of the *a*-GaN grown on *r*-sapphire by MOCVD, indicating the different types of defects. The cross-sectional images clearly show extensive TDs, BSFs terminated by PDs, and PSFs. The densities of the different defects in these samples are $\approx 4 \times 10^5 - 1 \times 10^6$ cm^{-1} for BSFs, $\sim 9 \times 10^{10}$ to 2×10^{11} cm^{-2} for PDs and $\sim 5 \times 10^3$ to 2×10^4 cm^{-1} for PSFs. The surface morphology of *a*-GaN/*r*-Sap is also shown in Figure 1(c), indicating a typical elongated comet-like features along *c*-directions. The diagonal lines along the atomic force microscopy (AFM) images are along the $+c$ $[0001]-$ direction and at 90 degrees the *m*-direction $[10\bar{1}0]$.

The ISB structures were then grown on co-loaded *a*-GaN-FS and *a*-GaN/*r*-Sap substrates. Figure 1 (d) schematically shows the detailed ISB structures grown for this investigation. The structures consisted of 20 periods of nominal GaN/$Al_{0.4}Ga_{0.6}N$ MQW heterostructrues on a 20 nm unintentionally doped (UID) GaN buffer layer. The number of QWs in the MQW stack is chosen so that the stack thickness is similar to the penetration depth in our attenuated total internal reflection absorption measurements that are described further below. Three different sets of

structures were grown, for which the thickness of GaN QWs were changed (3.0 nm, 3.3. nm and 3.7 nm). For all the structures, the thicknesses of the AlGaN quantum barriers (QBs) were kept constant at 3.0 nm. Out of the 3 nm QBs, the bottom and top 0.5 nm of the QBs were kept UID, while the innermost 2.0 nm of the AlGaN QBs were doped with Si (up to ~ 5×10^{19} cm^{-3}). The doping level was chosen to achieve high doping concentration to produce large intersubband absorption, while keeping the Fermi energy (E_F) for a 2D electron gas in a quantum well at least 100 meV below the intersubband transition energy to minimize the electron population of the first excited level in the MQW system. Details of the calculations are provided in the Supplemental Material [41].

The structures were then characterized using high-resolution x-ray diffraction (XRD), TEM/scanning TEM (STEM), AFM, and atom-probe tomography (APT). To evaluate the interface quality, the QW thicknesses, and characterization of the extended defects, a high-angle annular dark-field (HAADF) STEM was used. The TEM/STEM samples were prepared by focused ion beam (FIB) with a FEI Helios Dualbeam Nanolab 600 instrument. A ThermoFisher Talos G2 200X TEM/STEMw/ChemiSTEM EDS system operating at 200 kV was used to perform the microstructure and chemical element mapping. APT was also used to investigate the compositions and alloy distribution in the GaN/AlGaN heterostructures in 3D at the nanometer scale [42,43]. The needle shaped specialized APT samples were prepared using an FEI Helios 600 dual beam FIB instrument [44] and the analysis was performed in laser-pulse mode using a Cameca 3000X HR Local Electrode Atom Probe (LEAP). A laser wavelength of 532 nm, 13 ps pulse duration, 200 kHz repetition rate, 10 μm spot size, 0.5 nJ pulse energy, and detection rate of 0.02 atoms per pulse were used for the APT measurement analysis, while the sample base temperature was 30 K. The commercial IVAS^{TM} software was used to obtain the 3D reconstruction, where a geometrical

algorithm was used based on the initial radius and the shank angles of the prepared tips according to the images obtained from scanning electron microscopy (SEM) data [44].

Finally, the ISB absorption properties of the samples were measured using a Fourier-transform IR (FTIR) spectroscopy transmission setup equipped with a mercury cadmium telluride (MCT) infrared photodetector. The measurement setup schematic is shown in Fig. 2. Due to strong substrate absorption, we used evanescent excitation of the GaN/AlGaN QWs brought in optical contact with 350-μm-thick 45°-polished Ge prisms (attenuated total internal reflection absorption measurements). Given the refractive indices of GaN, nominal $Al_{0.4}Ga_{0.6}N$, and Ge are known to be, approximately, 2.25, 2.1, and 4.0 respectively and the light incident angle of 45˚ on the Ge/sample interface, we obtain that the intensity of the evanescent illumination extends approximately 0.2 μm into the MQW structure for the measurement wavelength range of 4-5 μm. Since the thicknesses of the MQW stack in our samples is in the range of 120-135 nm, a nearly uniform illumination of the MQWs is achieved. The ISB absorption spectra were obtained by normalizing TM-polarized transmission spectra with TE-polarized transmission spectra that provided a reference since TE-polarized light does not interact with ISB transitions. A Lorentz function was used to fit the ISB absorption spectra to obtain the peak energy and the spectral linewidth.

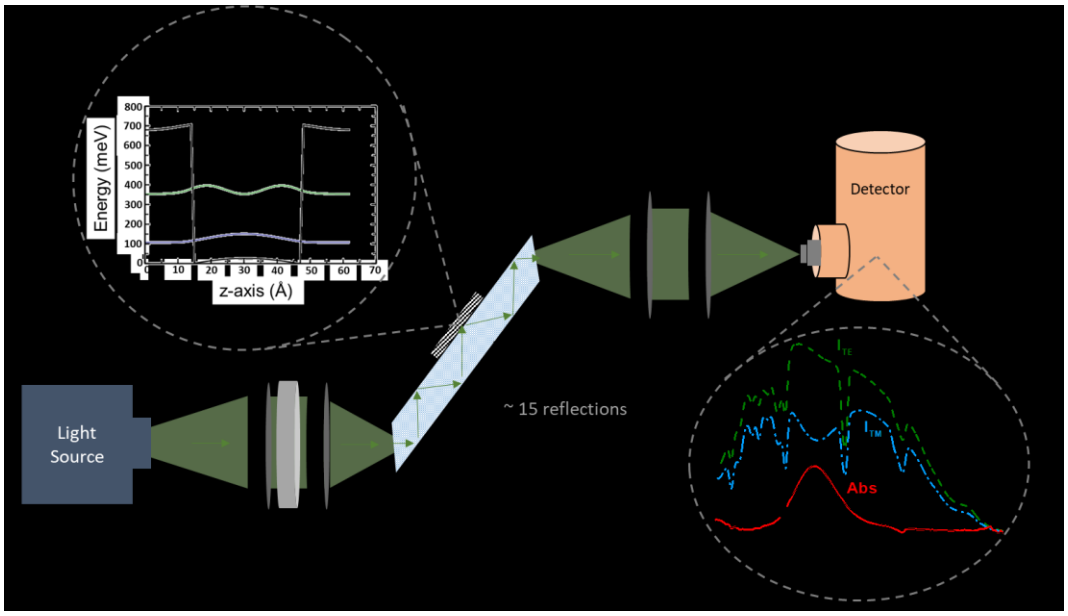

Figure 2. (a) Schematic of the setup to measure ISB absorption in our samples. The samples are placed epi-side-down onto an IR-transparent Ge prism. (b) Calculated conduction band diagram and square of electron wavefunctions of the first two quantum states for the MQW sample with a 3.3 nm QW width. The transmitted signal for two different polarization of the incident light (transverse electric, or TE and transverse magnetic, or TM) were captured. (c) Sample plots of the absorption spectra for TE-, TM-polarized incident light and the corresponding ISB absorption.

1. RESULTS AND DISCUSSIONS

Figure 3 shows the structural defects in GaN/AlGaN MQWs grown on *a*-GaN/*r*-Sap in the cross-section along $[1\bar{1}00]$ direction using two-beam bright field (BF) diffraction contrast (Figs. 3(a), 3(c) and 3(e)) and weak beam dark field (DF) diffraction contrast (Figs. 3(b) and 3(d)). The results indicate all dislocations are located in the *c*-plane. The TEM images illustrate the highly defective microstructure of the *a*-GaN/*r*-Sap including the ISB AlGaN/GaN QWs. While it is difficult to evaluate the accurate densities of different type of defects from these TEM images, we confirm that the *a*+*c* are in contrast with the partial dislocations for the g = 0002, while *a*+*c*, *a*, and 2/3 of all partial dislocations are in contrast for g = $11\bar{2}0$. The microstructure of the *a*-GaN/*r*-sap structures is similar to what has been reported much earlier in our group [45].

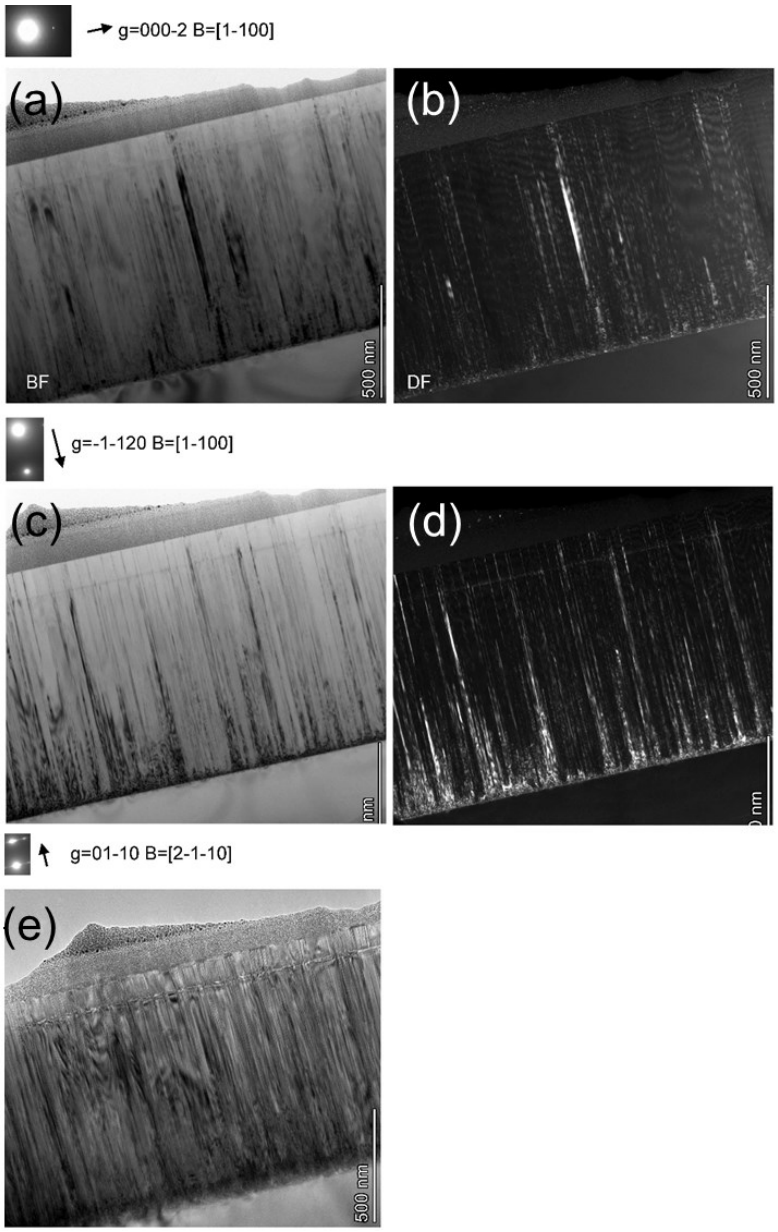

Figure 3. Cross sectional TEM images of a GaN/AlGaN MQW structures on *a*-GaN/*r*-Sap with (a,c,e) two-beam bright field (BF) diffraction contrast and (b,d) weak beam dark field (DF) diffraction contrast along (a,b) $g = 000\bar{2}$, (c,d) $g = \bar{1}\bar{1}20$, and (e) $g = 01\bar{1}0$. Note that the scale bars are the same for all the images.

Figure 4 compares the structural properties of the epilayers grown on *a*-GaN-FS and on *a*-GaN/*r*-Sap using high-resolution XRD ω-2θ scans and cross-sectional TEM. XRD data indicates sharp GaN peaks for the samples on *a*-GaN-FS (Fig. 4(a)), while much weaker GaN peaks are

observed for all the structures grown on *a*-GaN/*r*-Sap (two to three orders of magnitude lower peak intensity) (Fig. 4(b)). The MQW structures grown on *a*-GaN-FS also show more pronounced satellite (SL) peaks (five intense SL peaks) as shown in Fig. 4(a), which are normally observed for short-period superlattices [46]. In contrast, the structures grown on *a*-GaN/*r*-Sap only show four less pronounced SL peaks, as shown in Fig. 4(b). These results are indicative of higher interface abruptness for the structures grown on *a*-GaN-FS. The period of the SL peaks consistently reduces for thicker QW structures for both cases, consistent with larger periodicity of the superlattice structure. Cross-sectional HAADF-TEM (Fig. 4(c,d)) image comparison of selected samples from the superlattices with 3.0 nm QW width indicate a large difference in the densities of defects extended to the MQW heterostructures between the two structures, as expected from their extremely different substrate qualities.

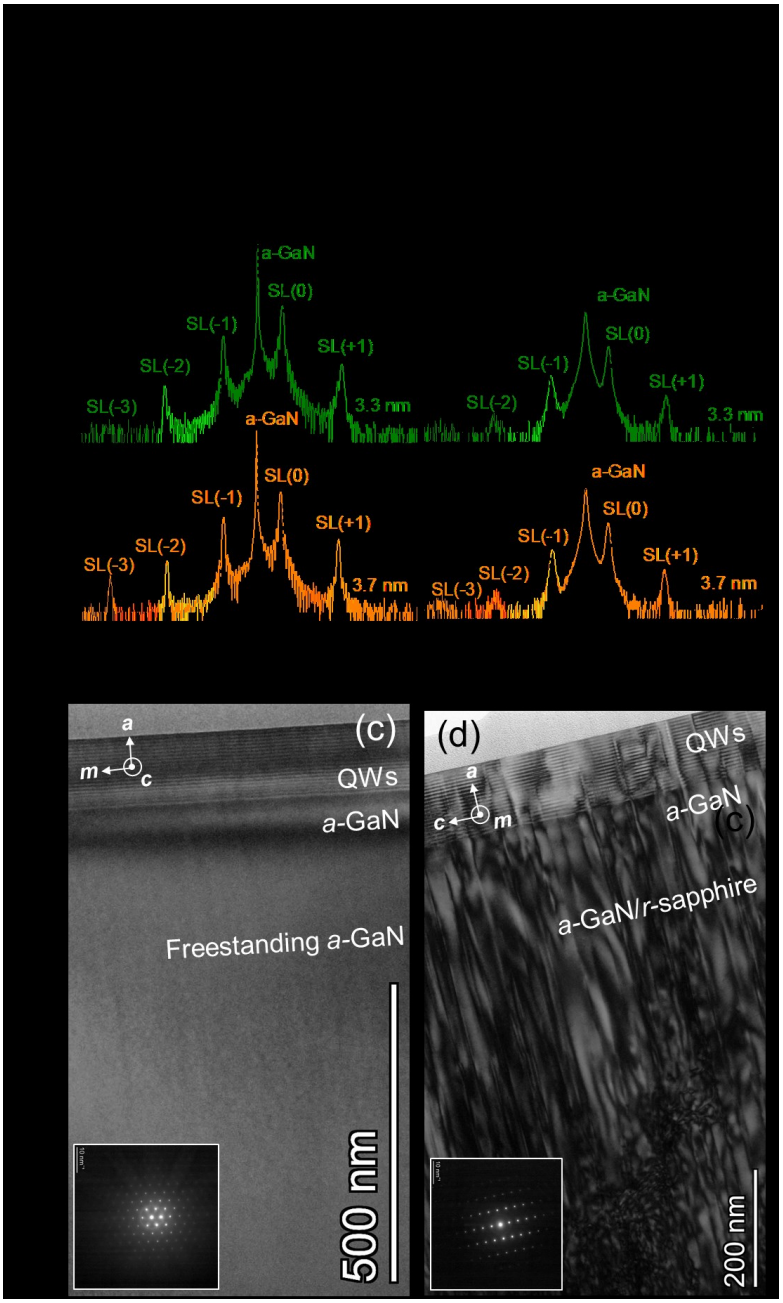

Figure 4. High-resolution (a,b) XRD omega 2-theta scans and (c,d) cross-sectional HAADF-TEM images of the structures on (a,c) *a*-GaN-FS and (b,d) *a*-GaN/*r*-Sap. Note that in the XRD measurements, the azimuthal angle has chosen such a way that the $(2\bar{2}04)$ *r*-Sapphire peak (at ~ 27.7°) is not captured. Also, note the difference in the axes of observation for the TEM images of (c) and (d), while the results are not dependent upon that.

The ISB optical transition properties, such as linewidth, can be strongly dependent on the interface abruptness. Hence, the interface quality and surface morphology of the structures for 3.0 nm QW width grown on *a*-GaN-FS and *a*-GaN/*r*-Sap were compared using cross-sectional STEM/EDS (Fig. 5) and AFM (Fig. 6). The structure grown on *a*-GaN-FS show a higher interface quality compared to the *a*-GaN/*r*-Sap sample. Also, the thickness of the QWs are slightly smaller for *a*-GaN-FS (~ 2.9-3.0 nm) compared to *a*-GaN/*r*-Sap (~ 3.1 to 3.2 nm) samples, while this could be a projection effect as the corrugated interface observed in the cross-section plane in Fig. 5 (*c*-plane) may also exist in the plane perpendicular to the cross-section plane at which the STEM image is taken. The AFM results (Fig. 6) also indicate a larger root-mean-square (RMS) roughness values for the *a*-GaN/*r*-Sap substrates (1.86 nm for 2×2 μm^2 scans) compared to the *a*-GaN-FS substrate (0.16 nm) and the corresponding ISB structure on *a*-GaN/*r*-Sap (2.3 nm) compared to the one grown on *a*-GaN-FS (0.3 nm). More detailed analysis of the AFM data can be found in the Supplemental Material [41].

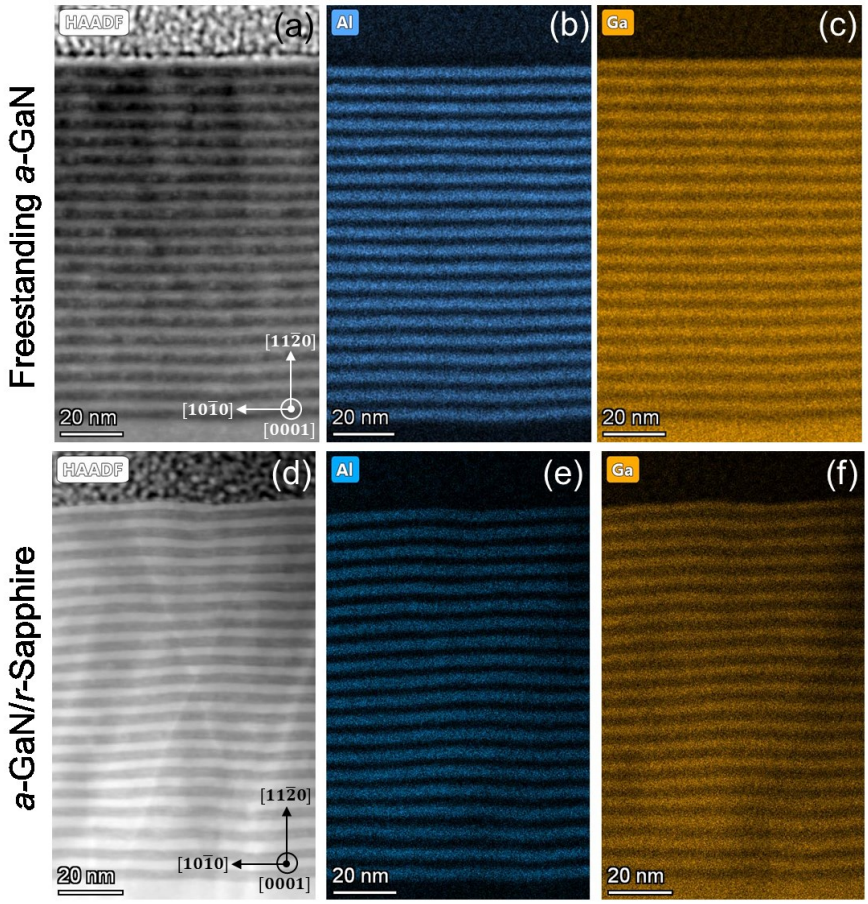

Figure 5. HAADF (a,d) cross-sectional STEM images across (0001) *c*-plane and corresponding (b,e) Al and (c,f) Ga elemental maps of GaN/AlGaN MQW heterostructures with 3.0 nm QWs grown by NH_3-MBE on (a-c) *a*-GaN-FS and (d-f) *a*-GaN/*r*-Sap substrates.

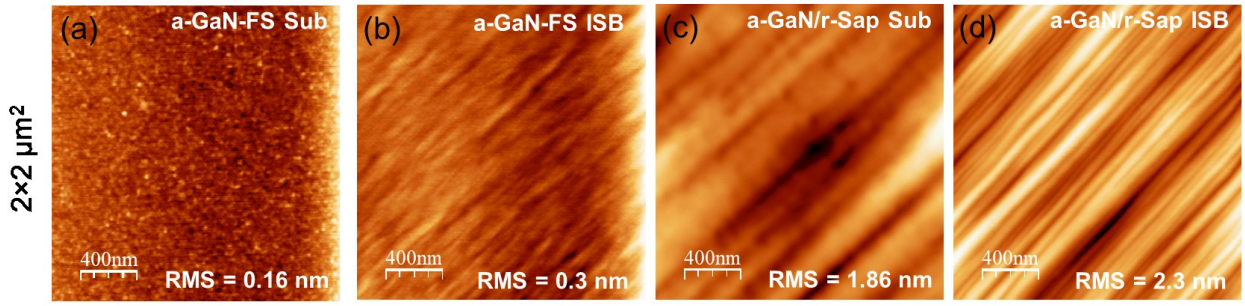

Figure 6. 2×2 µm^2 AFM images of (a) *a*-GaN-FS substrate, (b) ISB GaN/AlGaN heterostructures grown on *a*-GaN-FS substrate, (c) *a*-GaN/*r*-Sap substrate and (d) ISB GaN/AlGaN heterostructures grown on *a*-GaN/*r*-Sap substrate. Note that the elongated features observed on structures on *a*-GaN/*r*-Sap (c,d) are corresponding to the high density of stacking faults, while no elongated features are observed for the FS structures (a,b) (no stacking faults).

Figure 7 compares APT data and analysis of MQW samples with 3.0 nm QWs grown on *a*-GaN/*r*-Sap and *a*-GaN-FS substrates. According to the APT data, along the growth direction, the top interfaces between GaN and AlGaN (QW/QB interfaces) are slightly more abrupt than the bottom interfaces (Fig. 7), similar to our previous observations on other GaN/AlGaN MQW structures [12]. As shown in the variations of Ga/Al+Ga and Al/Al+Ga profiles along the growth directions (Figs. 7(b) and 7(f)), the Al fraction in the AlGaN layers varies in the range of 38-45% with ~ 8% deviation for the structure grown on *a*-GaN/*r*-Sap and in the range of 38-40% with ~ 4% deviation for the structure grown on *a*-GaN-FS. A normal Gaussian distribution of the Al atoms in the AlGaN QBs for the structure grown on *a*-GaN-FS (Fig. 7(h)) indicates a natural random alloy disorder without significant clustering with an average composition of ~ 30%. For the structure grown on *a*-Ga/*r*-Sap, however, the distribution of the Al atoms is not as symmetric and does not fully obey a Gaussian model (Fig. 7(d)), which indicates alloy clustering to some degree, while maintaining a similar average composition as that of the structure on *a*-GaN-FS.

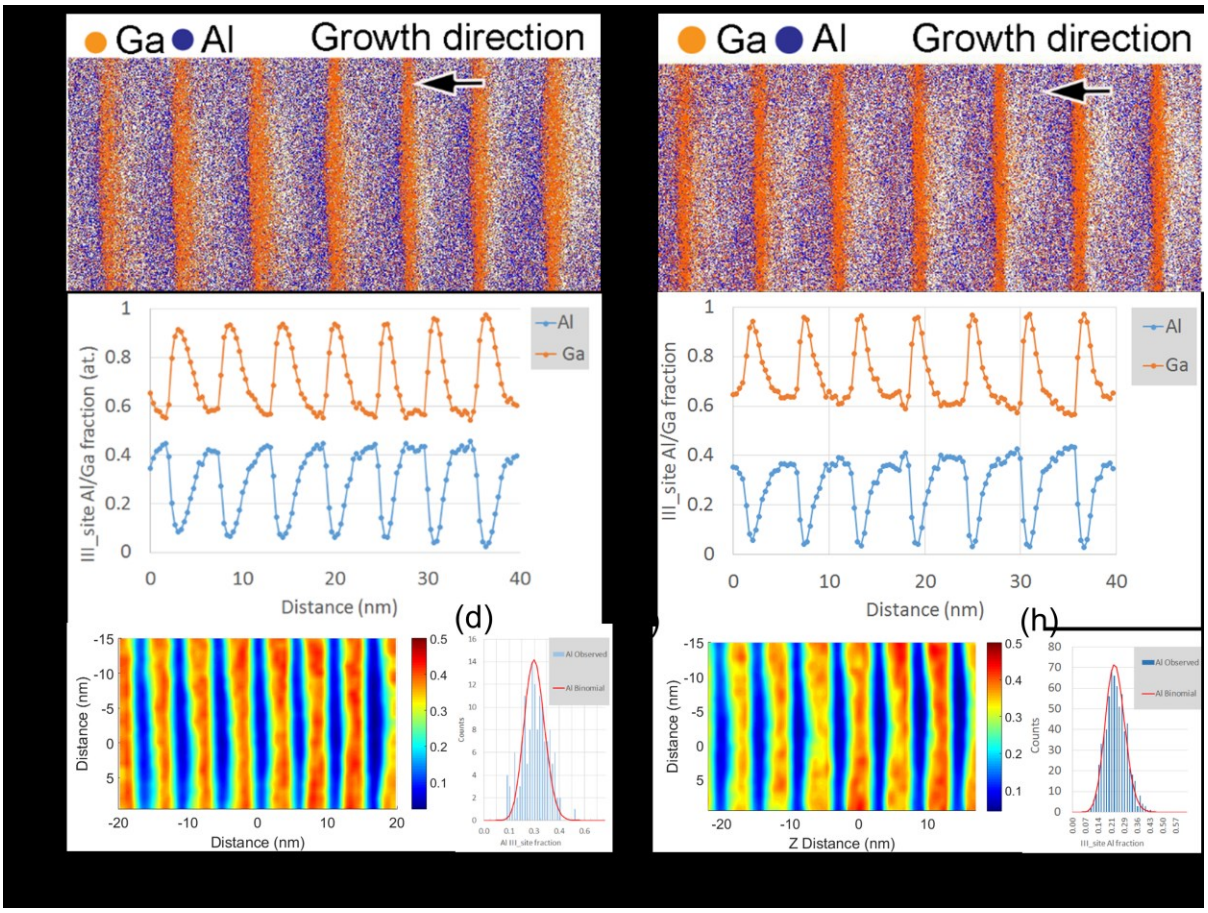

Figure 7. (a,e) APT data and analysis, (b,f) atomic line profiles of Ga and Al concentrations, (c,g) Al composition maps along the growth direction, and (d,h) distribution of the Al contents in the AlGaN QBs for the ISB structures containing a 20-period nonpolar *a*-plane GaN/AlGaN MQW heterostructures on (a-d) *a*-GaN/*r*-sapphire and (e-h) freestanding *a*-GaN. Note the difference in the distribution of Al contents in the barrier layers for the *a*-GaN/*r*-Sap sample compared to the *a*-GaN-FS, which may result in differences in the ISB absorption peak energy and linewidth.

The structures were then tested for optical absorption using an FTIR spectroscopy transmission setup described in Fig. 2. First, the transmitted intensity of the incident wide-band light source upon evanescently coupling to the MQW ISB structures were detected as a function of wavelength for TE and TM polarized incident light. The ISB absorption spectra were then computed by plotting $\ln(I_{TE}/I_{TM})$, where I_{TE} and I_{TM} correspond to the wavelength-dependent intensities of the transmitted light for TE- and TM-polarized light, respectively. Figure 8 compares the transmitted spectra and the obtained ISB absorption spectra for GaN/AlGaN heterostructures

grown on *a*-GaN-FS and on *a*-GaN/*r*-Sap for different QW widths. A Lorentz fitting was used to fit the experimental ISB absorption curves, which shows excellent fits for all the cases. Clear shifts of the absorption peak to lower energies are observed with increase of QW widths for both structures, resulting in a range resonance wavelength from ~ 250 – 300 meV (4 to 5 μm). Table II summarizes the experimental data displayed in Fig. 8.

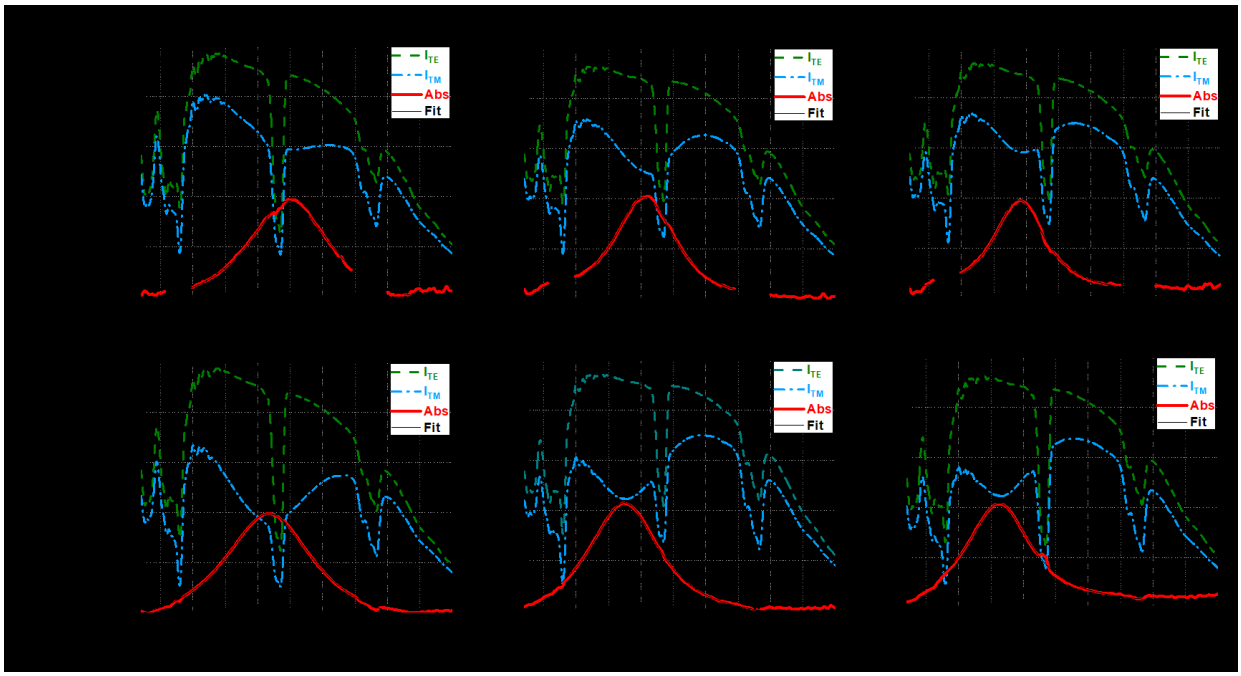

Figure 8. Transmission spectra for TE-polarized (green dashed line) and TM-polarized (blue dash-dotted line) incident light and the obtained ISB absorption spectra (thick red solid line) and the Lorentz function fitting curves (thin solid black line) for the MQW structures on (a-c) *a*-GaN-FS and (d-f) *a*-GaN/*r*-Sap with QW widths of (a,d) 3.0 nm, (b,e) 3.3 nm, and (c,f) 3.7 nm.

Table II summarizes the ISB absorption data demonstrated in Figure 8 and compares it to theoretically-computed values. Details of the calculations, that include many body effects, are described in Ref. [12] and the supplemental material to this reference. The calculations were performed using a shooting method in which a conduction band offset of 551 meV was used for $Al_{0.4}Ga_{0.6}N$/GaN system. The effective electron mass used in $Al_{0.4}Ga_{0.6}N$ and GaN were 0.264 m_0 and 0.22 m_0, respectively.

As expected from quantum mechanical calculations, wider QWs result in ISB transitions with lower energies for structures grown on both substrates (*a*-GaN-FS and *a*-GaN/*r*-Sap). However, for a given QW width, the co-loaded ISB structures grown on *a*-GaN/*r*-Sap show lower ISB transition energies than those grown on freestanding *a*-GaN-FS, which may be attributed to slightly thicker QWs (or different distribution of the Al content in the barrier) for the structures grown on *a*-GaN/*r*-Sap, as indicated in STEM results of Fig. 5. The slight difference in growth rate could be due to the difference in the surface and bulk properties of the highly defective substrates compared to the high-quality freestanding GaN. The ISB structures grown on *a*-GaN/*r*-Sap also show a 10-20% larger absorption linewidth compared to those grown on *a*-GaN-FS. However, despite the nearly 5 orders of magnitude difference in the defect densities for the two sample sets, the ISB absorption linewidth is not significantly different between the samples grown on the two different substrates. Therefore, the data demonstrates that unlike band-to-band transition devices, the ISB absorption is more tolerant to extended defects. We note that these findings are consistent with the recent results obtained for intersubband devices with As- and Sb-heterostructures grown foreign substrates [47,48]. The larger ISB absorption linewidths for the structures grown on *a*-GaN/*r*-Sap can be partially explained by the surface morphology (Fig. 6) and interface quality differences (Fig. 5). A systematic optimization of the growth conditions can improve the surface morphology of the *a*-GaN/*r*-Sap templates to further improve the interface quality and the ISB absorption properties. Given the manufacturing challenges of high-quality nonpolar GaN substrates, the low sensitivity of the ISB properties to the extended defects may provide a cost-effective and scalable approach for producing efficient ISB emitters in the mid- to far-IR using heteroepitaxial nonpolar III-nitride system on Sapphire and Si.

Table II. Experimentally measured and calculated ISB transition energies (E_{12} in meV) and absorption linewidths for the MQW GaN/AlGaN structures grown on *a*-GaN-FS and on heteroepitaxial *a*-GaN/*r*-Sap.

QW thickness	Samples grown on *a*-GaN-FS		Samples grown on *a*-GaN/*r*-Sap		Theoretical Energy (meV)
	Energy (meV)	Linewidth (meV)	Energy (meV)	Linewidth (meV)	With Many-Body
3.0 nm	299.1	80.7	283.5	87.4	299.25
3.3 nm	277.8	60.7	262.1	67.7	267.51
3.7 nm	269.6	48.4	256.2	59.6	233.13

2. SUMMARY AND CONCLUSIONS

In summary, we demonstrated a strong defect tolerance of GaN/AlGaN ISB structures grown on a nonpolar orientation. Comparison of two sets of samples grown on freestanding *a*-GaN and on *a*-GaN/*r*-Sapphire templates with at least 5 orders of magnitude difference in terms of densities of extended defects (BSFs, TDs, PDs, PSFs) indicate only 5% difference in the peak ISB absorption energies and only 10-20% difference in the ISB absorption linewidths. The structural data characterizations reveal the significant difference in the material quality, as well as surface, interface abruptness, alloy disorder and clustering for the two sample sets. Given the intrinsic properties of nonpolar III-nitrides for IR optoelectronics, our results are promising for the development of cost-effective, scalable, and highly-efficient mid- to far-IR optoelectronics using heteroepitaxial nonpolar III-nitrides.

3. ACKNOWLEDGMENT

This work was supported by the National Science Foundation (NSF) through Grant Nos. ECCS 1809691 and ECCS 1810318. Any opinions, findings, and conclusions or recommendations

expressed in this material are those of the author(s) and do not necessarily reflect the views of NSF. Additional support was provided by the Air Force Office of Scientific Research (Program No. FA9550-19-1-10090), DARPA NASCENT program, the Simons Foundation (Grant No. 601952, J.S.S.), and NSF-RAISE program (Grant No. A007231601). The authors acknowledge the support from the Solid-State Lighting and Energy Electronics Center (SSLEEC) at the University of California, Santa Barbara (UCSB). Samples were measured in the Microelectronics Research Center at the University of Texas at Austin, which is a member of the NSF National Nanotechnology Coordinated Infrastructure.

REFERENCES

[1] J. Faist, F. Capasso, D. L. Sivco, C. Sirtori, A. L. Hutchinson, and A. Y. Cho, *Quantum Cascade Laser*, Science **264**, 553 (1994).
[2] R. Paiella, *Intersubband Transitions In Quantum Structures* (McGraw-Hill Education, 2006).
[3] E. R. Weber, R. K. Willardson, and H. C. Liu, *Intersubband Transitions in Quantum Wells: Physics and Device Applications* (Academic Press, 1999).
[4] G. P. Agrawal and N. K. Dutta, *Semiconductor Lasers* (Springer Science & Business Media, 2013).
[5] J. Faist, *Quantum Cascade Lasers* (OUP Oxford, 2013).
[6] B. S. Williams, *Terahertz Quantum-Cascade Lasers*, Nat. Photonics **1**, 517 (2007).
[7] H. Morkoç, *Handbook of Nitride Semiconductors and Devices, Materials Properties, Physics and Growth* (John Wiley & Sons, 2009).
[8] E. Bellotti, K. Driscoll, T. D. Moustakas, and R. Paiella, *Monte Carlo Simulation of Terahertz Quantum Cascade Laser Structures Based on Wide-Bandgap Semiconductors*, J. Appl. Phys. **105**, 113103 (2009).
[9] G. Sun, J. B. Khurgin, and D. P. Tsai, *Spoof Plasmon Waveguide Enabled Ultrathin Room Temperature THz GaN Quantum Cascade Laser: A Feasibility Study*, Opt. Express **21**, 28054 (2013).
[10] N. Suzuki and N. Iizuka, *Feasibility Study on Ultrafast Nonlinear Optical Properties of 1.55-Mm Intersubband Transition in AlGaN/GaN Quantum Wells*, Jpn. J. Appl. Phys. **36**, L1006 (1997).
[11] M. Beeler, E. Trichas, and E. Monroy, *III-Nitride Semiconductors for Intersubband Optoelectronics: A Review*, Semicond. Sci. Technol. **28**, 074022 (2013).
[12] M. Monavarian, J. Xu, M. N. Fireman, N. Nookala, F. Wu, B. Bonef, K. S. Qwah, E. C. Young, M. A. Belkin, and J. S. Speck, *Structural and Optical Properties of Nonpolar M- and*

a-Plane GaN/AlGaN Heterostructures for Narrow-Linewidth Mid-Infrared Intersubband Transitions, Appl. Phys. Lett. **116**, 201103 (2020).
[13] E. J. Roan and S. L. Chuang, *Linear and Nonlinear Intersubband Electroabsorptions in a Modulation-doped Quantum Well*, J. Appl. Phys. **69**, 3249 (1991).
[14] K. Vijayraghavan, Y. Jiang, M. Jang, A. Jiang, K. Choutagunta, A. Vizbaras, F. Demmerle, G. Boehm, M. C. Amann, and M. A. Belkin, *Broadly Tunable Terahertz Generation in Mid-Infrared Quantum Cascade Lasers*, Nat. Commun. **4**, 1 (2013).
[15] J. Lee, M. Tymchenko, C. Argyropoulos, P.-Y. Chen, F. Lu, F. Demmerle, G. Boehm, M.-C. Amann, A. Alù, and M. A. Belkin, *Giant Nonlinear Response from Plasmonic Metasurfaces Coupled to Intersubband Transitions*, Nature **511**, 7507 (2014).
[16] J. Lee, N. Nookala, J. S. Gomez-Diaz, M. Tymchenko, F. Demmerle, G. Boehm, M.-C. Amann, A. Alù, and M. A. Belkin, *Ultrathin Second-Harmonic Metasurfaces with Record-High Nonlinear Optical Response*, Adv. Opt. Mater. **4**, 664 (2016).
[17] N. Nookala, J. Lee, M. Tymchenko, J. S. Gomez-Diaz, F. Demmerle, G. Boehm, K. Lai, G. Shvets, M.-C. Amann, A. Alu, and M. Belkin, *Ultrathin Gradient Nonlinear Metasurface with a Giant Nonlinear Response*, Optica **3**, 283 (2016).
[18] M. M. Fejer, S. J. B. Yoo, R. L. Byer, A. Harwit, and J. S. HarrisJr., *Observation of Extremely Large Quadratic Susceptibility at 9.6--10.8 \ensuremath{\mu}m in Electric-Field-Biased AlGaAs Quantum Wells*, Phys. Rev. Lett. **62**, 1041 (1989).
[19] I. Vurgaftman, J. R. Meyer, and L. R. Ram-Mohan, *Optimized Second-Harmonic Generation in Asymmetric Double Quantum Wells*, IEEE J. Quantum Electron. **32**, 1334 (1996).
[20] C. Sirtori, F. Capasso, J. Faist, L. N. Pfeiffer, and K. W. West, *Far-infrared Generation by Doubly Resonant Difference Frequency Mixing in a Coupled Quantum Well Two-dimensional Electron Gas System*, Appl. Phys. Lett. **65**, 445 (1994).
[21] B. Corcoran, C. Monat, C. Grillet, D. J. Moss, B. J. Eggleton, T. P. White, L. O'Faolain, and T. F. Krauss, *Green Light Emission in Silicon through Slow-Light Enhanced Third-Harmonic Generation in Photonic-Crystal Waveguides*, Nat. Photonics **3**, 4 (2009).
[22] C. Wang, Z. Li, M.-H. Kim, X. Xiong, X.-F. Ren, G.-C. Guo, N. Yu, and M. Lončar, *Metasurface-Assisted Phase-Matching-Free Second Harmonic Generation in Lithium Niobate Waveguides*, Nat. Commun. **8**, 1 (2017).
[23] M. Celebrano, X. Wu, M. Baselli, S. Großmann, P. Biagioni, A. Locatelli, C. De Angelis, G. Cerullo, R. Osellame, B. Hecht, L. Duò, F. Ciccacci, and M. Finazzi, *Mode Matching in Multiresonant Plasmonic Nanoantennas for Enhanced Second Harmonic Generation*, Nat. Nanotechnol. **10**, 5 (2015).
[24] N. Yu and F. Capasso, *Flat Optics with Designer Metasurfaces*, Nat. Mater. **13**, 2 (2014).
[25] A. V. Kildishev, A. Boltasseva, and V. M. Shalaev, *Planar Photonics with Metasurfaces*, Science **339**, (2013).
[26] R. W. Boyd, *Nonlinear Optics* (Academic Press, 2020).
[27] G. Li, S. Chen, N. Pholchai, B. Reineke, P. W. H. Wong, E. Y. B. Pun, K. W. Cheah, T. Zentgraf, and S. Zhang, *Continuous Control of the Nonlinearity Phase for Harmonic Generations*, Nat. Mater. **14**, 6 (2015).
[28] M. Monavarian, A. Rashidi, and D. Feezell, *A Decade of Nonpolar and Semipolar III-Nitrides: A Review of Successes and Challenges*, Phys. Status Solidi A **216**, 1800628 (2019).
[29] D. F. Feezell, J. S. Speck, S. P. DenBaars, and S. Nakamura, *Semipolar InGaN/GaN Light-Emitting Diodes for High-Efficiency Solid-State Lighting*, J. Disp. Technol. **9**, 190 (2013).

[30] A. E. Romanov, T. J. Baker, S. Nakamura, and J. S. Speck, *Strain-Induced Polarization in Wurtzite III-Nitride Semipolar Layers*, J. Appl. Phys. **100**, 023522 (2006).
[31] D. Feezell, Y. Sharma, and S. Krishna, *Optical Properties of Nonpolar III-Nitrides for Intersubband Photodetectors*, J. Appl. Phys. **113**, 133103 (2013).
[32] N. Suzuki and N. Iizuka, *Effect of Polarization Field on Intersubband Transition in AlGaN/GaN Quantum Wells*, Jpn. J. Appl. Phys. **38**, L363 (1999).
[33] A. Pesach, E. Gross, C.-Y. Huang, Y.-D. Lin, A. Vardi, S. E. Schacham, S. Nakamura, and G. Bahir, *Non-Polar m-Plane Intersubband Based InGaN/(Al)GaN Quantum Well Infrared Photodetectors*, Appl. Phys. Lett. **103**, 022110 (2013).
[34] C. Edmunds, J. Shao, M. Shirazi-HD, M. J. Manfra, and O. Malis, *Terahertz Intersubband Absorption in Non-Polar m-Plane AlGaN/GaN Quantum Wells*, Appl. Phys. Lett. **105**, 021109 (2014).
[35] C. B. Lim, A. Ajay, C. Bougerol, B. Haas, J. Schörmann, M. Beeler, J. Lähnemann, M. Eickhoff, and E. Monroy, *Nonpolarm-Plane GaN/AlGaN Heterostructures with Intersubband Transitions in the 5–10 THz Band*, Nanotechnology **26**, 435201 (2015).
[36] T. D. Moustakas and R. Paiella, *Optoelectronic Device Physics and Technology of Nitride Semiconductors from the UV to the Terahertz*, Rep. Prog. Phys. **80**, 106501 (2017).
[37] T. Kotani, M. Arita, and Y. Arakawa, *Observation of Mid-Infrared Intersubband Absorption in Non-Polar m-Plane AlGaN/GaN Multiple Quantum Wells*, Appl. Phys. Lett. **105**, 261108 (2014).
[38] J. Xu, M. Monavarian, N. Nookala, M. N. Fireman, K. S. Qwah, J. S. Speck, and M. A. Belkin, *Intersubband Transitions in GaN/Al0.5Ga0.5N Quantum Wells on a-Plane and m-Plane GaN Substrates*, in *2020 Conference on Lasers and Electro-Optics (CLEO)* (2020), pp. 1–2.
[39] M. Funato, M. Ueda, Y. Kawakami, Y. Narukawa, T. Kosugi, M. Takahashi, and T. Mukai, *Blue, Green, and Amber InGaN/GaN Light-Emitting Diodes on Semipolar {11-22} GaN Bulk Substrates*, Jpn. J. Appl. Phys. **45**, L659 (2006).
[40] K. Fujito, S. Kubo, and I. Fujimura, *Development of Bulk GaN Crystals and Nonpolar/Semipolar Substrates by HVPE*, MRS Bull. **34**, 313 (2009).
[41] See Supplemental Material at [URL will be inserted by publisher] for descriptions of post-processing of the experimental data and more detailed discussion of design considerations, including the effect of doping and number of QWs on the ISB properties.
[42] L. Rigutti, B. Bonef, J. Speck, F. Tang, and R. A. Oliver, *Atom Probe Tomography of Nitride Semiconductors*, Scr. Mater. **148**, 75 (2018).
[43] M. N. Fireman, B. Bonef, E. C. Young, N. Nookala, M. A. Belkin, and J. S. Speck, *Strain Compensated Superlattices on M-Plane Gallium Nitride by Ammonia Molecular Beam Epitaxy*, J. Appl. Phys. **122**, 075105 (2017).
[44] K. Thompson, D. Lawrence, D. J. Larson, J. D. Olson, T. F. Kelly, and B. Gorman, *In Situ Site-Specific Specimen Preparation for Atom Probe Tomography*, Ultramicroscopy **107**, 131 (2007).
[45] M. D. Craven, S. H. Lim, F. Wu, J. S. Speck, and S. P. DenBaars, *Structural Characterization of Nonpolar (11$\bar{2}$0) a-Plane GaN Thin Films Grown on (1$\bar{1}$02) r-Plane Sapphire*, Appl. Phys. Lett. **81**, 469 (2002).
[46] E. E. Fullerton, I. K. Schuller, H. Vanderstraeten, and Y. Bruynseraede, *Structural Refinement of Superlattices from X-Ray Diffraction*, Phys. Rev. B **45**, 9292 (1992).

[47] H. Nguyen-Van, A. N. Baranov, Z. Loghmari, L. Cerutti, J.-B. Rodriguez, J. Tournet, G. Narcy, G. Boissier, G. Patriarche, M. Bahriz, E. Tournié, and R. Teissier, *Quantum Cascade Lasers Grown on Silicon*, Sci. Rep. **8**, 1 (2018).

[48] R. Go, H. Krysiak, M. Fetters, P. Figueiredo, M. Suttinger, J. Leshin, X. M. Fang, J. M. Fastenau, D. Lubyshev, A. W. K. Liu, A. Eisenbach, M. J. Furlong, and A. Lyakh, *Room Temperature Operation of Quantum Cascade Lasers Monolithically Integrated onto a Lattice-Mismatched Substrate*, Appl. Phys. Lett. **112**, 031103 (2018).